

## Time dependence and local structure of tracer dispersion in oscillating liquid Hele-Shaw flows

Y. L. Roht, H. Auradou, J.-P. Hulin, D. Salin, R. Chertcoff, and I. Ippolito

Citation: *Physics of Fluids* **27**, 103602 (2015); doi: 10.1063/1.4932302

View online: <http://dx.doi.org/10.1063/1.4932302>

View Table of Contents: <http://scitation.aip.org/content/aip/journal/pof2/27/10?ver=pdfcov>

Published by the [AIP Publishing](#)

---

### Articles you may be interested in

[On the motion of unsteady translating bubbles in an unbounded Hele-Shaw cell](#)

*Phys. Fluids* **27**, 012102 (2015); 10.1063/1.4905582

[Experimental and numerical study of buoyancy-driven single bubble dynamics in a vertical Hele-Shaw cell](#)

*Phys. Fluids* **26**, 123303 (2014); 10.1063/1.4903488

[Two dimensional Leidenfrost droplets in a Hele-Shaw cell](#)

*Phys. Fluids* **26**, 032103 (2014); 10.1063/1.4867163

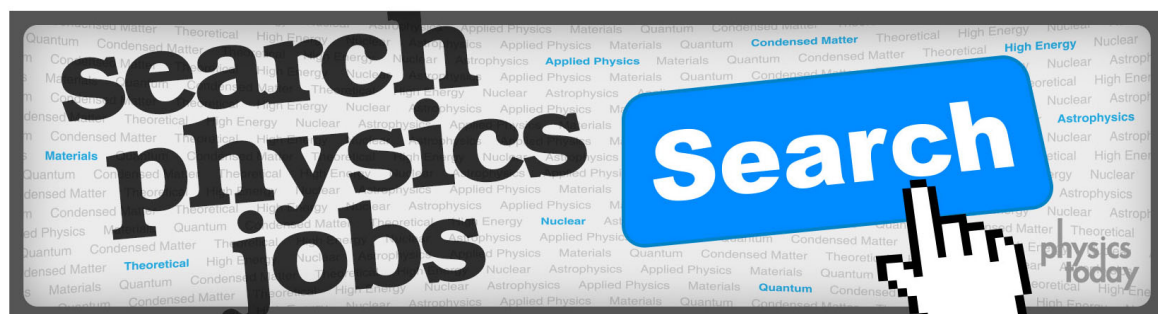
[Experimental study of dispersion and miscible viscous fingering of initially circular samples in Hele-Shaw cells](#)

*Phys. Fluids* **22**, 123104 (2010); 10.1063/1.3528039

[Stretching distributions in chaotic mixing of droplet dispersions with unequal viscosities](#)

*Phys. Fluids* **17**, 053101 (2005); 10.1063/1.1895798

---



# Time dependence and local structure of tracer dispersion in oscillating liquid Hele-Shaw flows

Y. L. Roht,<sup>1,a)</sup> H. Auradou,<sup>2,b)</sup> J.-P. Hulin,<sup>2,c)</sup> D. Salin,<sup>2,d)</sup> R. Chertcoff,<sup>1,e)</sup> and I. Ippolito<sup>1,f)</sup>

<sup>1</sup>*Grupo de Medios Porosos, Facultad de Ingeniería, Universidad de Buenos Aires, Paseo Colón 850, 1063 Buenos Aires, Argentina*

<sup>2</sup>*Univ. Paris-Sud, CNRS, Université Paris-Saclay, Lab. FAST, Bât 502, Campus Univ., Orsay F-91405, France*

(Received 19 March 2015; accepted 21 September 2015; published online 7 October 2015)

Passive tracer dispersion in oscillating Poiseuille liquid flows of zero net velocity is studied experimentally in a Hele-Shaw cell and numerically by  $2D$  simulations: this study is particularly focused on the time dependence and local properties of the dispersion. The dispersion mechanism is found to be controlled by the ratio  $\tau_m/T$  of the molecular diffusion time across the gap and the oscillation period (when molecular diffusion parallel to the flow is negligible). The  $2D$  numerical simulations complement the experiments by providing the local concentration  $c(x, z, t)$  at a given distance  $z$  from the cell walls (instead of only the average over  $z$ ). Above a time lapse scaling like  $\tau_m$ , the variation of  $c$  with the distance  $x$  along the flow becomes a Gaussian of width constant with  $z$  while the mean distance  $\bar{x}$  may depend both on  $z$  and  $t$ . For  $\tau_m/T \lesssim 2$ , the front spreads through Taylor-like dispersion and the normalized dispersivity scales as  $\tau_m/T$ . The front oscillates parallel to the flow with an amplitude constant across the gap; its width increases monotonically at a rate modulated at twice the flow frequency, due to variations of the instantaneous dispersivity. For  $\tau_m/T \gtrsim 20$ , the molecular diffusion distance during a period of the flow is smaller than the gap and the normalized dispersivity scales as  $(\tau_m/T)^{-1}$ . The oscillations of the different points of the front follow the local fluid velocity: this produces a reversible modulation of the global front width at twice the flow frequency and in quadrature with that in the Taylor-like regime. © 2015 AIP Publishing LLC. [<http://dx.doi.org/10.1063/1.4932302>]

## I. INTRODUCTION

The dispersion of miscible solutes or tracers in parallel or quasi-parallel laminar flows is of interest in many applications like chemical engineering, microfluidics, chromatography, or separation and has been extensively studied in the case of stationary flows since the classical pioneering papers of Taylor<sup>1</sup> and Aris.<sup>2</sup> In such flows, the so-called *Taylor dispersion* corresponds to a balance between molecular diffusion across the flow lines and the convective spreading of the tracer due to velocity gradients transverse to the main flow; the corresponding dispersion coefficient is proportional to the square of the characteristic velocity  $U$  unlike for  $3D$  random porous media for which geometrical dispersion proportional to  $U$  is dominant. For a flow between two parallel planes (spacing  $H$ ), Taylor dispersion is the relevant mechanism provided the Péclet number  $Pe = UH/D_m$  is

a) Electronic mail: [lucreroht@gmail.com](mailto:lucreroht@gmail.com)

b) Electronic mail: [auradou@fast.u-psud.fr](mailto:auradou@fast.u-psud.fr)

c) Electronic mail: [hulin@fast.u-psud.fr](mailto:hulin@fast.u-psud.fr)

d) Electronic mail: [salin@fast.u-psud.fr](mailto:salin@fast.u-psud.fr)

e) Electronic mail: [ricardochertcoff@gmail.com](mailto:ricardochertcoff@gmail.com)

f) Electronic mail: [i.ippolito@conicet.gov.ar](mailto:i.ippolito@conicet.gov.ar)

larger than  $\approx 30$  ( $D_m$  is the molecular diffusivity); at lower Péclet numbers, pure molecular diffusion is dominant.

Fewer research has been devoted to dispersion in pure (zero mean velocity) oscillatory flows. These are however of significant interest in such applications as pulmonary ventilation flows or flows induced by surface waves (for instance, in shallow water in estuaries). On the fundamental side, pure oscillating flows raise important questions in relation to the well known reversibility of the flow fields at low Reynolds numbers when the mean flow is reversed: can this reversibility result in a very low instantaneous dispersion after an integral number of oscillations of the flow velocity? Does spreading remain diffusive?

In a pioneering work, Aris<sup>3</sup> applied his method of moments to longitudinal dispersion induced by a pulsating viscous flow in an infinite tube, but with a nonzero time averaged velocity. The transition between the irreversible and reversible regimes in Taylor dispersion was studied experimentally<sup>4</sup> by means of a step-like point injection of tracer at the center of two parallel square plates (spacing  $H$ ) followed by a reversal of the flow after a preselected variable time. This same problem was investigated theoretically<sup>5</sup> by an irreversible thermodynamics approach. These studies demonstrated the major influence of the ratio  $\tau_m/T$  of the characteristic time  $\tau_m = H^2/D_m$  for molecular diffusion between the plates to the interval  $T$  between the beginning of the injection and its reversal: there is indeed a transition from irreversibility to partial reversibility as  $\tau_m/T$  increases. For oscillating flows,  $\tau_m/T$  will also be a key parameter ( $T$  is this time the period of the oscillations).

Watson<sup>6</sup> discussed theoretically tracer diffusion for pure oscillating flows in a circular tube or between parallel plates: he determined the relevant characteristic numbers of the problem and predicted the value of the macroscopic diffusion coefficient after a stationary diffusive regime has been reached. Experimental verifications of these predictions were reported by Joshi *et al.*<sup>7</sup> and Kurzweg *et al.*<sup>8,9</sup> for oscillating gas flows in circular tubes with a nonzero mean velocity. These latter works are concerned with the macroscopic effective diffusivity averaged over the whole flow section and measured after a stationary diffusive regime is reached. Regarding this last point, several authors considered the variation with time of the dispersion and not just its asymptotic value at long times. Holley *et al.*<sup>10</sup> showed that, in estuaries, the effective diffusion coefficient is strongly reduced when the width reaches about 200 m, which also is the case for many waterways: a possible explanation is the partial reversibility of dispersion in oscillating flows at high enough frequencies. Chatwin<sup>11</sup> demonstrated the occurrence of second harmonics of the flow frequency in the time dependence of the dispersion. He also suggested that, in the case of blood flow, there might be a transition from Taylor to partly reversible dispersion for vessels of internal diameter larger than about 2 mm. Yasuda<sup>12</sup> studied dispersion when an oscillatory boundary layer is present: he compared the results to those obtained for a steady flow and explained why, in the oscillatory case, the apparent dispersion coefficient may appear to decrease when the flow is reversed.<sup>13,14</sup> For turbulent flows, some results obtained for laminar flows may be transposed by replacing the molecular diffusion coefficient by the eddy diffusivity.<sup>15,16</sup>

The above works on oscillatory flows are mostly concerned with the regimes achieved at long times and, in all cases, with the macroscopic dispersion (averaged over the gap of the flow channel). They do not provide information on the local mechanisms of this type of dispersion and its partial reversibility. The objective of the present paper is, therefore, to relate the variations with time of the local concentration to those of the global dispersion. For this purpose, we study experimentally and numerically at both the macroscopic and local scales the different diffusive spreading regimes in oscillating flows between parallel plane walls and determine their domains of existence and their time dependence.

We discuss first experiments performed in a Hele-Shaw (HS) geometry by optical measurements of the average of the concentration of a dye tracer over the gap of the cell. We study whether the spreading of the tracer is diffusive and the variation of the corresponding macroscopic diffusion coefficient  $D_{||}$  with the amplitude and frequency of the oscillations for fluids of different viscosities: these variations can be collapsed onto a single master curve by using proper dimensionless variables such as the ratio  $\tau_m/T$ .

Numerical 2D Monte Carlo simulations in a parallel plate geometry allow us to study the spatial distribution of the tracer in the gap of the cell and its dependence on time. More specifically,

we compare in both regimes the variation with time of the first and second moment of the local concentration distribution along the flow at different distances from the walls. Another important issue is the time necessary to achieve diffusive spreading and its relation to the characteristic diffusion time. In the [Appendix](#), we show that the analytical results of Chatwin<sup>11</sup> and Watson<sup>6</sup> can be adapted to the present configuration and provide a basis of comparison for both the experimental and numerical results obtained at the macroscopic scale.

## II. EXPERIMENTAL SETUP AND PROCEDURE

The fluid flows inside a Hele-Shaw cell (Figs. 1(a) and 1(b)) made of two transparent glass plates ( $400 \times 70 \times 10$  mm) separated by a Mylar sheet of appropriate geometry providing a gap of thickness  $H = 0.4 \pm 0.02$  mm with an internal width of 50 mm in its parallel part.

For short periods  $T$ , the flow is generated by applying an oscillating motion to the piston of a syringe by means of a rotating crank driving a rod and hooked up through a 1/40 reduction gear to a dc motor rotating at a constant rate: the corresponding range of  $T$  values is  $2 \leq T \leq 80$  s. Longer periods ( $25 \leq T \leq 250$  s) are obtained by means of a programmable syringe pump (Harvard type 22): the sine wave time dependence of the flow rate is approximated by a variation by discrete steps of minimum individual duration 0.7 s (each period  $T$  of variation contains therefore at least 35 points and the flow rate never goes to zero). We checked that this discretization does not perturb the dispersion process by comparing results obtained in the range of  $T$  values where both devices can be used: the results obtained are indeed identical within experimental error (see Fig. 5 below).

The fluids used in the experiments are aqueous solutions of glycerol at concentrations equal to 21% and 50% with respective viscosities of 1.8 and 6 mPa s (at 20 °C). All the experiments were performed at a constant temperature of 20 °C. Water Blue dye<sup>17</sup> at a concentration of 2.0 g/l is added to one of the solutions as a passive tracer. The molecular diffusion coefficient  $D_m$  of the dye, as determined through independent measurements and results from the literature,<sup>18,19</sup> is  $D_m = 4.05 \times 10^{-4}$  mm<sup>2</sup>/s for the 21% glycerol solution.

The cell is illuminated from below and the concentration field  $C(x, y, t)$  is determined from images acquired by a digital CCD camera placed above the setup (Roper Coolsnap FX):  $C(x, y, t)$  is the average, over the gap  $H$  of the cell, of the local concentration  $c(x, y, z, t)$ . Each image contains  $1300 \times 140$  pixels with a depth of 12 bits. The field of view is  $289 \times 31$  mm and the resolution is 4.5 pixels/mm. For each experiment, 650 images are acquired at time intervals from 0.2 to 12.5 s.

Prior to each experiment, reference images are obtained with the cell saturated by the transparent solution and, then, by the pure dyed one (dye concentration  $C_o$ ). For each experimental image, the intensity  $I_{C(x,y)}$  of the transmitted light measured for each pixel of coordinates  $(x, y)$  is then converted into the corresponding concentration  $C(x, y, t)$  with the help of the reference images and of a calibration curve.<sup>19-21</sup> This curve relates the relative concentration of dye  $C/C_o$  to the

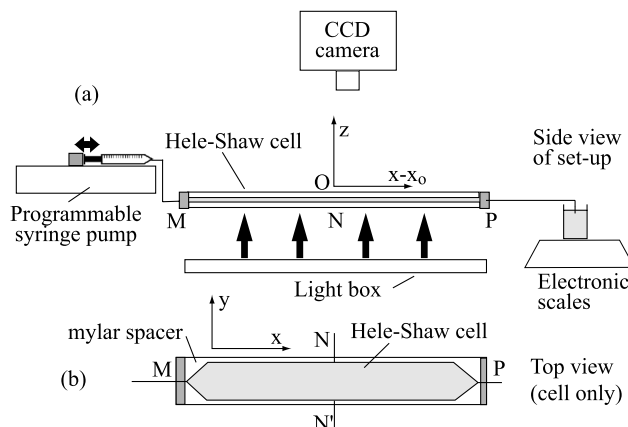


FIG. 1. Schematic views of the cell and of the experimental setup. (a) Side view of the global experimental setup; (b) top view of the Hele Shaw cell.

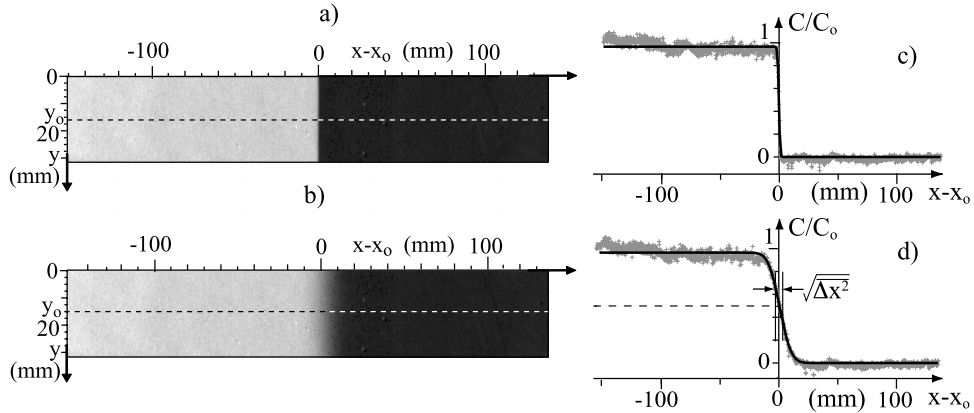


FIG. 2. Left: Images of the cell and corresponding tracer concentration map after image processing (a) at  $t_0 = 0$  (b) at  $t_1 = 300$  s. The fluid oscillates with a period  $T = 9$  s and an amplitude (averaged over the gap)  $A = 2$  mm. Right: Profiles of the variation of the concentration  $C(x, y_0, t)$  with the distance  $x - x_0$  to the initial location of the front at the same time  $t$  as the facing image and at a same transverse distance  $y_0 = 15$  mm. Fits by Eq. (3) are superimposed as continuous lines onto the experimental curves ( $x_0(t_1) = 157$  mm and  $\Delta x^2(t_1) = 55$  mm<sup>2</sup>).

relative optical absorbance of the model,

$$\frac{A(C)}{A(C_0)} = \frac{\ln\langle I_t/I_C \rangle_{x,y}}{\ln\langle I_t/I_{C_0} \rangle_{x,y}}, \quad (1)$$

where  $\langle I_t/I_C \rangle_{x,y}$  and  $\langle I_t/I_{C_0} \rangle_{x,y}$  are the spatial averages of the ratios of the transmitted intensity when the model is saturated by the transparent solution (no dye) and by solutions of respective concentrations  $C$  or  $C_0$ . This ratio is determined through independent measurements for different concentrations  $C$  (constant in the model) ranging from 0.1 to 2 g/l. The relation between  $A(C)/A(C_0)$  and  $C/C_0$  is then approximated by a third order polynomial using coefficients determined by a fit to the calibration data; these coefficients are assumed to remain the same at the local scale for determining the relative concentration  $C(x, y)/C_0$ .

At the beginning of the experiment ( $t = 0$ ), each half of the cell length is saturated with one of the fluids with a sharp relative concentration variation at the front (Fig. 2(a)): this is obtained by injecting simultaneously the two fluids at the ends  $M$  and  $P$  of the cell and letting them flow out together on the two side ports  $N$  and  $N'$  in the middle (Fig. 1). The initial front coincides with the line  $NN'$ . The side ports are then shut off and the injection device is connected to the inlet  $M$ . The variations of the flow rate are monitored from the variations of the weight of a beaker connected to the outlet  $P$  which are well fitted by a sine wave. This measurement, together with the area of the cell section, gives the amplitude  $A$  (averaged over the gap) of the displacement of the fluid in the constant width part of the cell: the values in the present work range from  $A = 2$  to 6 mm. Images of the cell are then acquired at regular intervals. Assuming that the mean displacement of the fluid varies as  $A \sin(\omega t)$  with  $\omega = 2\pi/T$ , the average fluid velocity satisfies

$$\langle v_x(z, t) \rangle_z = \omega A \cos(\omega t) = U \cos(\omega t). \quad (2)$$

In the following,  $U = \omega A = 2\pi A/T$  is used as the characteristic velocity of the problem. Since, due to the oscillations, the average displacement of the fluid is zero, the total travelled distance  $x_{tr}$  is characterized here by the integral of the absolute value  $|d\bar{x}/dt|$  of the front velocity between times 0 and  $t$ ; for an integral number  $N$  of periods,  $x_{tr} = 4NA$ .

### III. EXPERIMENTAL RESULTS

#### A. Time dependence of the mean front profile

Figures 2(a) and 2(b) display experimental maps of the normalized dye concentration  $C(x - x_0)/C_0$  at times  $t_0 = 0$  and  $t_1 = 300$  s ( $C_0$  is the concentration of the pure dyed solution); the

width of the front is clearly larger in the latter case. Here and below, we use  $x - x_o$  as the horizontal scale (the initial location  $x_o$  of the front is indeed the physically relevant origin of the coordinate  $x$ ).

Profiles of  $C(x, y_o)/C_o$  corresponding to the same times as in Figs. 2(a) and 2(b) and to  $y = y_o = 15$  mm are plotted in Figs. 2(c) and 2(d): curve (d) is well fitted by the error-like function (continuous black line),

$$C(x, y_o) = \frac{1}{2} \left[ 1 - \operatorname{erf} \left( \frac{x - \bar{x}(y_o, t)}{\sqrt{2 \Delta x^2(y_o, t)}} \right) \right]. \quad (3)$$

This fit provides the values of the mean coordinate of the front  $\bar{x}$  and its mean square width  $\overline{\Delta x^2}$ . This procedure is preferred to a direct computation from the experimental curves because it is less sensitive to noise and to small variations of the measured values corresponding to  $C = 0$  and  $C_o$  far from the front.

Figures 3(a) and 3(b) display spatiotemporal diagrams of the respective variations of  $\bar{x}(y, t) - x_o$  and  $\overline{\Delta x^2}(y, t)$ ;  $\bar{x}(y, t)$  oscillates with time at the frequency of the oscillations of the flow (alternate light and dark stripes) and is practically independent of  $y$ , as shown by the very good overlay of the 5 different local profiles in Fig. 3(c) and the perfectly vertical patterns in Fig. 3(a). This shows that the average over  $z$  of the component  $v_x$  of the flow velocity is constant with  $y$ .

The mean square width  $\Delta x^2$  increases globally linearly with time at all distances  $y$  (Fig. 3(d)) and the slope of the local profiles is equal to that of the global one to within 10%. Front spreading in the direction  $x$  of the flow is therefore globally diffusive and can be described by the coefficient  $D_{\parallel} = (1/2)d\overline{\Delta x^2}/dt$ . An additional modulation at half the period  $T$  of the flow is superimposed onto this linear trend (continuous global curve in Fig. 3(d)); this modulation is more clear and is visible during a longer time on the global profile than on the local ones (the period is rather  $T$  than  $T/2$  in some areas as shown by the distribution/length of the vertical stripes in Fig. 3(b)). This may reflect dye exchange due to secondary flow components in the  $y$  direction.

In the following, we use a 1D description leaving aside the variations with  $y$  and study the properties of the averages over  $y$  of  $\bar{x}(t)$  and  $\overline{\Delta x^2}(t)$ ; their variations during one period  $T$  are

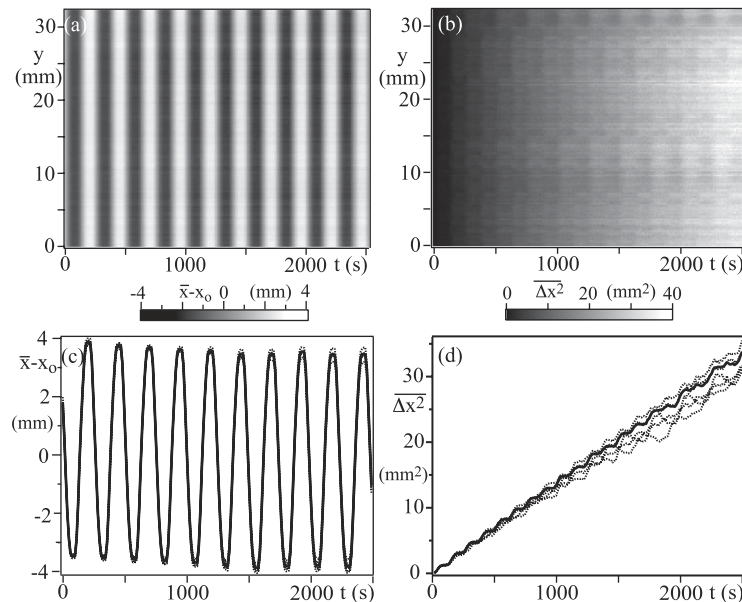


FIG. 3. (a) and (b) Spatiotemporal diagrams of (a) the mean distance  $\bar{x}(y, t) - x_o$  (grayscale) and (b) the width  $\overline{\Delta x^2}(y, t)$  (grayscale) of the front as a function of the time  $t$  (horizontal scale) and of the transverse distance  $y$  (vertical scale); (c) and (d) Variations with time, for the same experiment as graphs (a) and (b), of  $\bar{x}(t)$  and  $\overline{\Delta x^2}$  averaged over the full width of the cell (continuous line) and over 5 sets of 10 adjacent lines centered respectively at  $y = 2.5, 10, 17.5, 25,$  and  $32.5$  mm (dotted lines);  $T = 250$  s,  $A = 3.5$  mm.

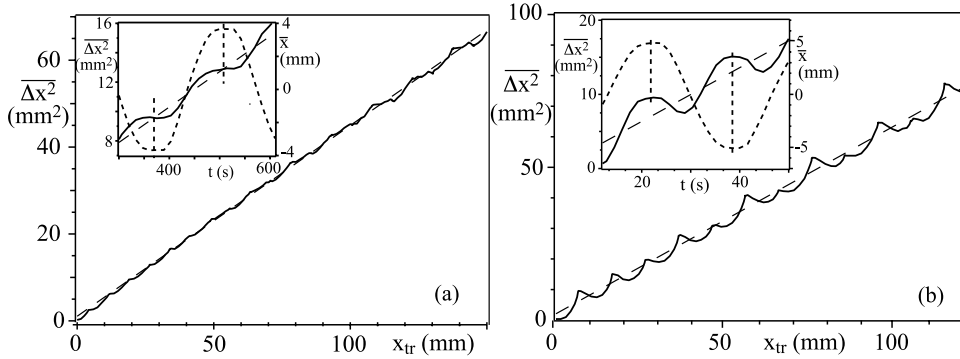


FIG. 4. Variations of the mean square width  $\overline{\Delta x^2}$  of the front and of the mean distance  $\bar{x}$ . Main graphs: variation of  $\overline{\Delta x^2}$  as a function of the travelled distance  $x_{tr}$  (continuous line) and linear fit of this variation (dashed line). Insets: variations as a function of time of  $\bar{x}$  (curved dotted line),  $\overline{\Delta x^2}$  (continuous line), and linear fit (dashed line); vertical dotted lines: extrema of  $\bar{x}$ . (a)  $T = 250$  s,  $A = 3.5$  mm; (b)  $T = 33$  s,  $A = 5$  mm.  $H = 0.4$  mm,  $\tau_m = 395$  s.

compared in the insets of Fig. 4(c) for  $T = 250$  and  $T = 33$  s. Like in Figs. 3(c) and 3(d), the variation of  $\bar{x}(t)$  is sinusoidal of period  $T$  and that of  $\overline{\Delta x^2}(t)$  combines a global linear increasing trend and a periodic variation of period  $T/2$ .

For  $T = 250$  s (a),  $\overline{\Delta x^2}$  increases continuously, but at a varying rate going to zero, like the velocity, at the extremal values of  $\bar{x}(t)$  (vertical dotted lines in the inset). The modulation is less apparent and the linear trend is more clear when  $\overline{\Delta x^2}$  is plotted (main graph) as a function of the travelled distance  $x_{tr}$ .

For  $T = 33$  s (b),  $\overline{\Delta x^2}$  decreases instead when the flow direction is reversed before increasing again (inset). This modulation at twice the frequency of the flow is, this time, also very visible in the variation of  $\overline{\Delta x^2}$  with  $x_{tr}$  (main graph in Fig. 4(b)). Experimental, numerical, and analytical results on the amplitude and phase of these modulations will be discussed in Sec. V B (see Fig. 13).

These results show that tracer spreading is fully irreversible for oscillations of large periods  $T$  (it always increases with time), but partly reversible for shorter periods  $T$  (it decreases during a fraction of the period). Over time lapses longer than  $T$ ,  $\overline{\Delta x^2}$  increases linearly in both regimes both with time and  $x_{tr}$  which demonstrates the diffusive character of the spreading. As pointed above, the corresponding 1D diffusion coefficient is equal to  $D_{\parallel} = \Delta(\overline{\Delta x^2})/(2\Delta t)$ , ( $\Delta(\overline{\Delta x^2})$  is the variation during a time lapse  $\Delta t \gg T$ ).

## B. Dimensionless variables characterizing the front diffusion

Assume, in an homogeneous medium, a uniform flow of velocity  $U$  parallel to  $x$  and an initial macroscopic concentration  $C(x, 0)$  of the tracer independent of  $y$ ;  $C(x, t)$  will remain constant with  $y$  at all times and satisfies the 1D Gaussian dispersion relation,

$$\frac{\partial C}{\partial t} = U \frac{\partial C}{\partial x} + D_{\parallel} \frac{\partial^2 C}{\partial x^2}. \quad (4)$$

For a constant mean flow velocity  $\langle v_x \rangle_z = U$ , solutions of this equation are given by Eq. (3) with  $\bar{x} = Ut$  and  $\overline{\Delta x^2} = 2D_{\parallel} t$ .

In the case of a stationary plane Poiseuille flow of velocity  $v_x(z) = (3U/2)(1 - 4z^2/H^2)$  between parallel plates (spacing  $H$ ), front spreading becomes diffusive at the macroscopic scale for  $t \gg \tau_m$  ( $\tau_m = H^2/D_m$ ). Then, the concentration  $C(x, t)$  satisfies Eq. (4) and the coefficient  $D_{\parallel}$  is given by<sup>1,2</sup>

$$D_{\parallel} = \frac{U^2 H^2}{210 D_m} + D_m = \frac{U^2 \tau_m}{210} + D_m. \quad (5)$$

Eq. (5) is a macroscopic relation and  $C(x, t)$  is the average of the local microscopic concentration  $c(x, z, t)$  over the distance  $z$  inside the cell gap; the local concentration  $c(x, z, t)$  satisfies instead the local microscopic equation,

$$\frac{\partial c}{\partial t} = v_x(z) \frac{\partial c}{\partial x} + D_m \Delta c. \quad (6)$$

The term proportional to  $U^2$  in Eq. (5) corresponds to Taylor dispersion already mentioned in Sec. I. Physically, it represents the diffusion coefficient associated to a random walk with individual steps of duration  $\sim \tau_m$  and velocity  $\sim U$ : the transverse diffusion time  $\tau_m$  characterizes indeed the Lagrangian decorrelation of the velocity of the tracer particles as they diffuse across the streamlines. The term  $D_m$  of Eq. (5) corresponds to pure molecular diffusion parallel to the flow. The ratio of the first and second term is  $Pe^2/210$  in which the Péclet number is  $Pe = UH/D_m$ : the influence of pure molecular diffusion is therefore only significant at low Péclet numbers (typically below 30).

In the present experiments, for very large oscillation periods such that  $T \gtrsim \tau_m$ , we can assume that Eq. (5) is satisfied for a velocity  $U(t) = \langle v_x(z, t) \rangle_z$  equal to  $U \cos(\omega t)$  (Eq. (2)). The mean square width of the front satisfies the relation  $d\overline{\Delta x^2}/dt = 2D_{\parallel}(U(t))$  which, using Eqs. (2) and (5) and integrating with respect to time, leads to

$$\frac{\overline{\Delta x^2}(t)}{A^2} = \frac{\pi}{210} \frac{\tau_m}{T} (\sin(2\omega t) + 2\omega t) + \frac{2t}{\tau_m} \left(\frac{H}{A}\right)^2. \quad (7)$$

This result agrees with the predictions of Refs. 6 and 11 (see Eq. (A9)). The last term on the right corresponds to pure molecular diffusion and the others to Taylor dispersion. This expression predicts variations of  $\overline{\Delta x^2}(t)$  with time that are globally linear with a modulation of the slope at a frequency equal to twice that of the flow; this slope is always positive and has a minimum close to zero for  $t/T = n/2 + 1/4$ . All these features are visible on the experimental curve of Fig. 4(a) (inset).

The mean global dispersion coefficient  $D_{\parallel}$  given by the linear increasing trend of Eq. (7) over time lapses  $\Delta t \gg T$  is

$$D_{\parallel} = \frac{\pi^2 A^2 \tau_m}{105 T^2} + D_m. \quad (8)$$

The normalized dispersivity  $l_D/A = D_{\parallel}/UA$  has then the dimensionless form,

$$\frac{l_D}{A} = \frac{\pi}{210} \frac{\tau_m}{T} + \frac{1}{2\pi} \left(\frac{H}{A}\right)^2 \frac{T}{\tau_m}. \quad (9)$$

The second, pure molecular diffusion term is only important at very low Péclet numbers  $UH/D_m$  and we show in Sec. IV that it is negligible in the present experiments. Eq. (9) involves then only the dimensionless variables  $l_D/A = D/(UA)$  and  $t/\tau_m$ .

### C. Experimental variation and scaling law for the dimensionless dispersivity

The experimental values of  $l_D/A = D_{\parallel}/UA$  are plotted in Fig. 5 as a function of  $\tau_m/T$ . We note first the good collapse of the different experimental points for all values of  $A$ ,  $\mu$ , and  $T$ : this confirms the relevance of the choice of dimensionless variables. Data points in the range  $25 \leq \tau_m/T \leq 80$  correspond to both setups used to generate the oscillating flows; they coincide within experimental error for same  $\tau_m/T$  values which shows that the variation of the flow rate of the programmable pump by discrete steps does not influence dispersion.

For  $\tau_m/T \leq 3$ , the trend of the data is compatible with the variation  $l_D/A \propto \tau_m/T$  predicted by Eq. (9) for the Taylor dispersion regime. When  $\tau_m/T$  increases,  $l_D/A$  reaches a maximum and decreases then roughly as  $(\tau_m/T)^{-1}$  for  $\tau_m/T \geq 15$  (dashed line).

This latter scaling law can be retrieved as follows. Consider a half-period  $T/2$  during which the flow keeps the same orientation (Fig. 6); the characteristic diffusion distance of tracer particles along  $z$  is  $\Delta z_d \sim (D_m T)^{1/2} \ll H$ . The corresponding spreading  $|\Delta x_c|$  of the front due to the velocity gradient  $\partial v_x/\partial z$  may be estimated by  $|\Delta x_c| \sim |\Delta z_d (\partial v_x/\partial z) T| \sim (D_m T)^{1/2} U T/H$ . In Taylor

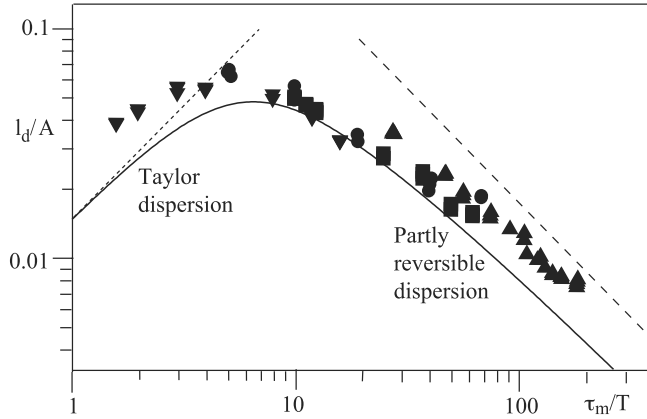


FIG. 5. Experimental variation in log-log coordinates of the normalized dispersivity  $l_D/A$  as a function of the normalized inverse oscillation period  $\tau_m/T$  for different oscillation amplitudes and fluid viscosities.  $\mu = 1.8$  Pa. s: ( $\blacktriangledown$ )  $A = 3.5$  mm; ( $\blacktriangle$ )  $A = 5$  mm; ( $\bullet$ ):  $A = 6$  mm. ( $\blacksquare$ ):  $\mu = 6$  Pa. s,  $A = 5$  mm. Continuous line: predictions from Ref. 6 (see the Appendix); dotted line: prediction from Eq. (9); dashed line: slope  $-1$ .

dispersion at a constant flow, the transition from convective to macroscopically diffusive spreading takes place at a time of the order of  $\tau_m$  representing the characteristic Lagrangian decorrelation time (see Sec. III B). For  $\tau_m/T \gtrsim 20$ ,  $\tau_m$  must be replaced by  $T$  (decorrelation is induced in this case by the flow reversal instead of molecular diffusion across the gap  $H$ ). We must have then also  $|\Delta x_c| \simeq (D_{\parallel}T)^{1/2}$ . Equating the two expressions of  $|\Delta x_c|$  and taking again  $A \sim UT$  lead to the scaling relations,

$$\frac{D_{\parallel}}{D_m} \sim \left(\frac{A}{H}\right)^2 \tag{10}$$

or

$$\frac{l_D}{A} \sim \left(\frac{\tau_m}{T}\right)^{-1}. \tag{11}$$

Eq. (11) predicts well the experimental variation for  $\tau_m/T \gtrsim 15$  (Fig. 5). Analytical results from Ref. 6 (see the Appendix) are also plotted in Fig. 5 (continuous line): the transition between the limiting regimes occurs at the same value of  $\tau_m/T$  as experimentally. The experimental and analytical values of  $l_D/A$  are similar for  $8 \leq \tau_m/T \leq 50$ ; the experimental values are slightly larger above and below this range; this may be due to the variations of the distribution of the tracer in the  $y$  direction observed in Figs. 3(b)-3(d).

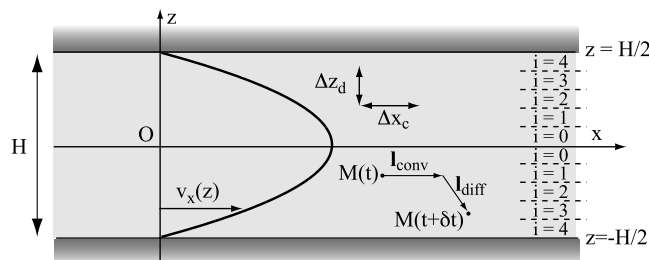


FIG. 6. Schematic view of the fluid velocity field  $v_x(z)$  and of the motion of the tracer particles.  $\Delta z_D$ : transverse diffusion distance during a half-period  $T/2$ ;  $\Delta x_c$ : corresponding spreading distance resulting from the velocity gradient  $\partial v_x/\partial z$ . Numerical Monte Carlo simulation:  $M(t)$  and  $M(t+\delta t)$  respective locations of a tracer particle at times  $t$  and  $t+\delta t$ ;  $\mathbf{l}_{conv}$  = deterministic convective displacement during one time step  $\delta t$ ;  $\mathbf{l}_{diff}$  = diffusive displacement during one time step resulting from the Brownian motion. At the right: numbering of the different slices used in the simulations.

## IV. 2D MONTE CARLO SIMULATIONS OF DISPERSION IN OSCILLATING FLOWS BETWEEN PARALLEL PLATES

### A. Physical hypothesis and procedure of the Monte Carlo simulation

Both the experiments and the analytical predictions<sup>6,11</sup> deal with averages of the concentration over the gap: this is adequate in low frequency regimes ( $\tau_m/T \lesssim 1$ ), for which the concentration distribution in the gap is homogenized by molecular diffusion at all times during the period  $T$ , but not in the high frequency one. Numerical simulations are needed to visualize the distribution of the “tracer particles” inside the gap and determine the variations of dispersion with the distance  $z$ : this allows us to understand the local mechanisms of the dispersion process. These simulations determine, in addition, the time necessary to reach a stationary dispersion regime, as well as the prefactors in the expression of the dispersivity. Here, we use Monte Carlo simulations considering a set of “particles” moving independently under the combined effects of convection and molecular diffusion.<sup>22</sup>

In oscillating flows between parallel solid walls, there appears near each wall, at high frequencies, a viscous boundary layer corresponding to a transition between a region of velocity constant with  $z$  in the center part of the gap and a zero velocity at the walls.<sup>23,24</sup> The thickness  $\delta_v$  of this layer increases at low frequencies with  $\delta_v = (\nu T/\pi)^{1/2}$  so that

$$\frac{\delta_v}{H} = \sqrt{\frac{T}{\tau_m} \frac{\nu}{\pi D_m}}, \quad (12)$$

where  $\delta_v$  becomes therefore of the order of  $H$  if  $\tau_m/T \simeq \nu/3D_m$ . For periods  $T$  large compared to this limiting value, this oscillating velocity boundary layer does not exist any more and one recovers the Poiseuille profile with a parabolic velocity variation with distance in the gap. In the present work,  $\nu/\pi D_m$  is of the order of 1000 for the less viscous solution and still larger for the higher viscosity one; the maximum value of  $\tau_m/T$  is 1000, so that  $\delta_v/H > 1$  and the velocity profile may be assumed to be a Poiseuille one.

At  $t = 0$ , all particles are released on the line  $x = 0$  and are distributed uniformly in the gap. This corresponds to a pulse injection of the tracer instead of a step-like one in the experiments but profiles corresponding to a step-like injection might also be used. The location of all particles is updated after each time step (duration  $\delta t$ ). The new location  $\mathbf{OM}(t + \delta t)$  is related to the previous one  $\mathbf{OM}(t)$  by (Fig. 6)

$$\mathbf{OM}(t + \delta t) = \mathbf{OM}(t) + \delta \mathbf{l}_{conv} + \delta \mathbf{l}_{dif} = \mathbf{v} \delta t + \sqrt{6D_m \delta t} \mathbf{u}. \quad (13)$$

$\delta \mathbf{l}_{conv}$  corresponds to the convection at the instantaneous Poiseuille flow velocity  $\mathbf{v}(z, t)$  parallel to the axis  $x$  and  $\delta \mathbf{l}_{dif}$  to the random Brownian motion due to molecular diffusion.<sup>22</sup> The orientation of the unit vector  $\mathbf{u}$  is distributed uniformly in all directions and varies at random from one particle or one time step to another. The time step  $\delta t$  is selected for a given value of  $D_m$  so that the last term  $\mathbf{l}_{dif}$  on the right side of Eq. (13) is small compared to  $H$  (the numerical results were checked to be robust with respect to this choice). Zero flux boundary conditions on the upper and lower surfaces of the cell are implemented by reflecting on the walls particles moving outside the fluid volume. The sequence of convective and diffusive displacements is repeated for a minimum of 30 periods in order to check the stationarity of the spreading process (generally a smaller number of periods is displayed for better visibility).

At each time step, we compute, from the distribution of the particles (Figs. 9(a) and 9(b)), the histograms of their coordinates  $x$  (Figs. 9(c) and 9(d)). These histograms are either computed for all particles (upper curves) or separately for 10 different slices of thickness  $\Delta y = a/10$ ; the two histograms corresponding to same absolute values of  $|y|$  are then combined with indices  $i$  (Fig. 6). The global mean square width  $\overline{\Delta x^2}$  and mean distance  $\bar{x}$  are determined by fitting the global histogram by the Gaussian law,

$$P(x) = \frac{C}{\sqrt{2\pi\overline{\Delta x^2}}} e^{-\frac{(x - \bar{x})^2}{2\overline{\Delta x^2}}}, \quad (14)$$

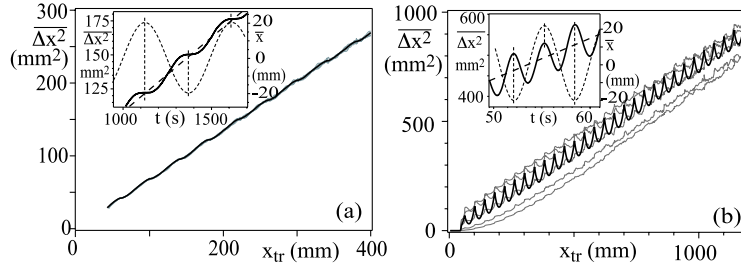


FIG. 7. Variation of  $\overline{\Delta x^2}$  (main graph and inset) and  $\bar{x}$  (inset) with the travelled distance  $x_{tr}$  (main graph) and with time (inset) for the distribution of particles in 2D numerical simulations. Thick black lines: widths of histograms computed over the gap of thickness  $H$  of the cell. Thinner grey lines: widths of histograms computed over 5 pairs of slices of index  $i$  increasing from the lower to the upper grey curves (Fig. 7(b)). Dashed line: linear fit for the variation of  $\overline{\Delta x^2}$  with time; curved dotted line: variation of  $\bar{x}$ ; vertical dotted lines: extrema of  $\bar{x}$ . (a)  $T = 500$  s,  $\tau_m/T = 0.8$ ; (b)  $T = 6.66$  s,  $\tau_m/T = 60$ ; (a) and (b):  $A = 20$  mm,  $D_m = 4 \cdot 10^{-4}$  mm<sup>2</sup> s<sup>-1</sup>.

in which  $C$  is a constant; this method is used for consistency with the analysis of the experimental results and in order to reduce the influence of the noise in the histograms.

## B. Numerical results for global dispersion characteristics

The variations of  $\bar{x}$  are displayed in Figs. 7(a) and 7(b) (insets) and 11(a) and 11(b) (black lines) for two values of  $\tau_m/T$  corresponding to the two different dispersion regimes discussed above. Like in the experiments (insets of Figs. 4(a) and 4(b)),  $\bar{x}$  oscillates at the frequency of the flow with an amplitude close to  $A$ : this variation and those  $\bar{x}^i$  for individual slices are discussed in Sec. V.

The variations of  $\overline{\Delta x^2}$  with  $x_{tr}$  and  $t$  are shown in Figs. 7(a) and 7(b) and display the same features as the experimental curves of Figs. 4(a) and 4(b). In the Taylor regime (case (a) with  $\tau_m/T = 0.8$ ), dispersion always increases with time and the variation levels off when the flow velocity goes to zero (inset of Fig. 7(a)). In the partly reversible dispersion regime,  $\overline{\Delta x^2}$  decreases instead when the flow direction changes (inset of Fig. 7(b)). These features are interpreted in Sec. V B. The variation of  $\overline{\Delta x^2}$  with  $x_{tr}$  displays only a weak modulation in the first regime but a clear one in the second. Over time lapses  $\gg T$ ,  $\overline{\Delta x^2}$  increases linearly with time: a linear regression provides, like in the experiments,  $D_{\parallel}$  and  $l_D$ .

Figure 8 compares, for three values of  $A/H$ , the variations of  $l_D/A$  with  $\tau_m/T$  obtained in this way (open symbols) to analytical results from Ref. 6 (continuous lines). The numerical values corresponding to different amplitudes  $A$  collapse perfectly for  $\tau_m/T \geq 1$  (like for the experimental data) and there is a perfect agreement between these values and the predictions from Ref. 6 (continuous lines).

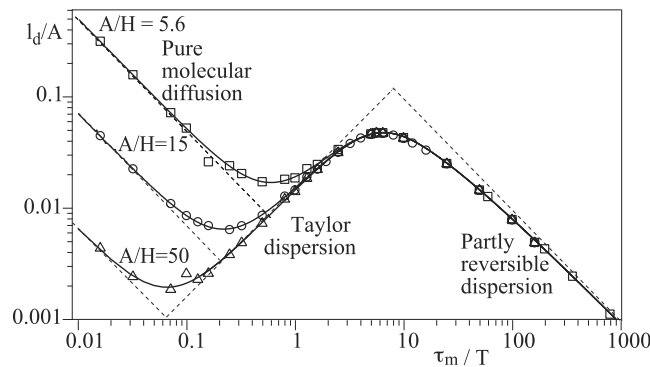


FIG. 8. Numerical and analytical variations of the normalized dispersivity  $l_D/A$  with the ratio  $\tau_m/T$  for different oscillation amplitudes. Numerical simulations (open symbols): ( $\square$ )  $A = 2.25$  mm ( $A/H = 5.6$ ); ( $\circ$ )  $A = 6$  mm ( $A/H = 15$ ); ( $\triangle$ )  $A = 20$  mm ( $A/H = 50$ );  $H = 0.4$  mm,  $D_m = 4 \times 10^{-4}$  mm<sup>2</sup> s<sup>-1</sup>. Continuous line: predictions from Ref. 6. Dotted lines  $l_d/A \propto \tau_m/T$  or  $(\tau_m/T)^{-1}$ .

At the lowest values of  $\tau_m/T$ , the numerical/analytical variations corresponding to different values of  $A/H$  do not coincide any more. This range corresponds to low velocities for which pure longitudinal molecular diffusion is dominant (this domain was not explored in the experiments). Eq. (9) reduces then to  $l_d/A = (T/2\pi\tau_m)(H/A)^2$ . In this regime,  $l_D/A$  is therefore proportional to  $(\tau_m/T)^{-1}$  and to  $(A/H)^{-2}$  (see Fig. 8). The transition between the pure molecular diffusion and Taylor regimes takes place when the two terms of Eq. (9) are equal, *i.e.*, for  $\tau_m/T = (H/A)(\sqrt{105}/\pi)$ : the value of  $\tau_m/T$  at the transition varies then as  $H/A$  (Fig. 8).

For  $\tau_m/T \simeq 2$ , the value of  $l_d/A$  for  $A/H = 5.6$  still falls on the common trend corresponding to Taylor dispersion: since these are the lowest values of  $\tau_m/T$  and  $A/H$  in our experiments, this justifies, *a posteriori*, the hypothesis of a negligible longitudinal molecular diffusion.

We explain now the above results (particularly regarding the oscillations of the dispersion) by comparing the motion and dispersion of tracer particles in several slices at different transverse distances  $z$ .

## V. SPATIAL VARIATION IN THE GAP OF THE TRACER DISPERSION AND MEAN VELOCITY

### A. Global trend of front-width time variation at different locations in the gap

As a first step, we compare the variations of the dispersion in the different slices over time lapses that are long compared to the period  $T$  and for an integer (or half-integer) number of oscillations: this removes asymmetries induced by the fluid displacement (see Figs. 10(a)-10(c)). Figs. 9(a) and 9(b) display distributions in the partial reversibility regime ( $\tau_m/T = 200$ ) at two different times equal, respectively, to  $0.04\tau_m$  and  $0.3\tau_m$  (*i.e.*,  $8T$  and  $60T$ ).

At the shorter time, the distribution of the coordinates  $x$  of the particles is broader near the walls than in the middle of the gap: this agrees with the discussion of Sec. III C since the velocity gradients are larger near the walls. This is confirmed by comparing the local histograms of the values of  $x$  (lower curves in Fig. 9(c)): they are narrower for slice 0 in the middle of the gap (black curve) than for slice 4 near the walls (grey curve). As a result, the global distribution (upper black curve) is not well fitted by a Gaussian variation (dotted line). At the longer time, instead, the histograms corresponding to the different slices nearly coincide and both the local and global histograms are Gaussian (Figs. 9(b)-9(d)).

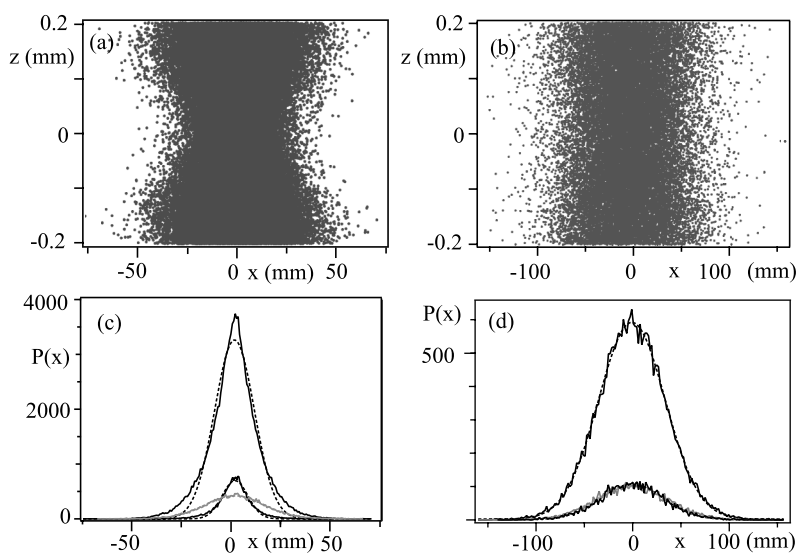


FIG. 9. ((a) and (b)) Distribution of the tracer particles in the gap between the cell walls after two different numbers of oscillations  $N=7.5$  (a) and  $N=60$  (b).  $\tau_m/T=200$ ;  $A=20$  mm;  $H=0.4$  mm;  $D_m=4 \cdot 10^{-4}$  mm<sup>2</sup> s<sup>-1</sup>. ((c) and (d)) Corresponding histograms of the number of particles as a function of the distance  $x$ , in the whole gap (upper black curve) and in slices 0 (lower black curve) and 4 (grey curve) (see Fig. 6). Dotted lines are Gaussian fits.

This explains the variations of  $\overline{\Delta x^2}$  with  $x_r$  for different slices in Fig. 7(b): while  $\overline{\Delta x^2}$  is initially much larger near the walls (like in Figs. 9(a)-9(c)), the variations of  $\Delta x^2$  for the different slices become then linear and parallel so that their *relative* difference gets small (Figs. 9(b)-9(d)). The transition towards the linear regime occurs after a time  $t \sim \tau_m/4$ , roughly independent of  $\tau_m/T$  for  $\tau_m/T \gtrsim 20$ . The relevance of  $\tau_m$  as the proper characteristic time is checked by increasing  $D_m$  which reduces, as expected, the transition time by the same factor.

In the Taylor-like regime ( $\tau_m/T \lesssim 2$ ), the distributions of the particles in all slices become Gaussian and identical after a time  $t \ll T$  (they look then like those of Figs. 9(b)-9(d)): this accounts for the overlap, in Fig. 7(a), of the curves corresponding to different slices.

## B. Global and local oscillations of $\bar{x}$ and $\overline{\Delta x^2}$

Figure 10 compares, in the two spreading regimes, the distributions of the tracer particles at three times corresponding to an integer number of periods ((b) and (e)) and to a quarter of period before ((a) and (d)) and after ((c) and (f)); the fluid displacement is therefore extremal for ((a), (c), (d), and (f)). For  $\tau_m/T = 60$  (partial reversibility regime) ((a)-(c)), the *local* width  $\Delta x_f$  of the “cloud” of particles is the same at all distances  $z$  and increases very little from (a) to (c); the *global* width is instead larger in cases (a) and (c) than in case (b) by an amount  $\Delta x_c$  and appears to follow the *local* displacement of the fluid (zero at the walls). For  $\tau_m/T = 0.8$  (Taylor-like regime) ((d)-(f)), there is no such distortion of the geometry of the front (and no additional “convective” increase  $\Delta x_c$  of its width): it remains straight and follows the “global” oscillations of the fluid at the average of its velocity over the gap.

Quantitatively, Figs. 11(a) and 11(b) compare the variations with time of the mean displacements  $\bar{x}(t)$  and  $\bar{x}^i(t)$  in the full gap and in each slice  $i$  for these two same values of  $\tau_m/T$ .

For  $\tau_m/T = 0.8$  (Taylor-like regime) (a), the variation with time of the global mean distance  $\bar{x}(t)$  and those of  $\bar{x}^i(t)$  coincide perfectly visually for all slices. The amplitude of these oscillations is constant with time and identical to better than 1%; the phase shift with respect to the oscillations of the fluid is zero within measurement error ( $\lesssim 3^\circ$ ). For  $\tau_m/T = 60$  (partial reversibility regime) (b), the oscillations reach a constant amplitude after a time of the order of  $\tau_m/10$ . Unlike for the Taylor regime, the amplitudes of the local displacements  $\bar{x}^i$  differ from  $\bar{x}$  and decrease as one moves away

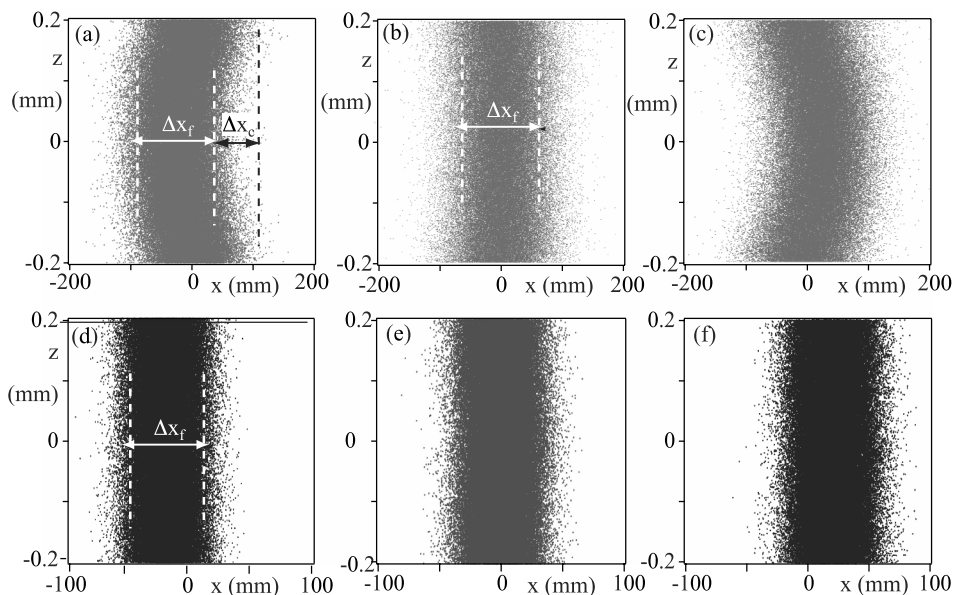


FIG. 10. Distribution of the particles in the gap at three different times for  $\tau_m/T = 60$  ((a)–(c)) and  $\tau_m/T = 0.8$  ((d)–(f)): (a)  $t = 19.75T$ ; (b)  $t = 20T$ ; (c)  $t = 20.25T$ ; (d)  $t = 4.75T$ ; (e)  $t = 5T$ ; (f)  $t = 5.25T$ .  $A = 20$  mm;  $H = 0.4$  mm;  $D_m = 4.05 \cdot 10^{-4} \text{ mm}^2 \text{ s}^{-1}$ .

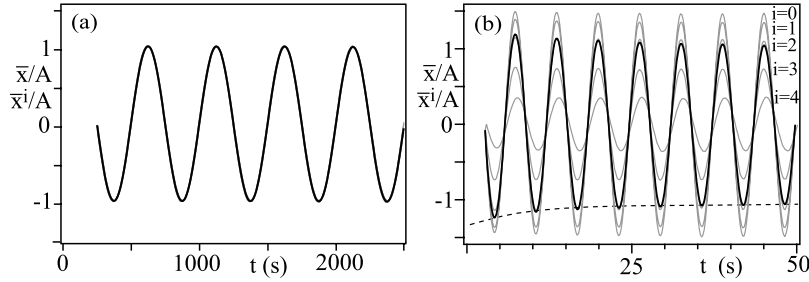


FIG. 11. Superimposed time variations of the mean displacements  $\bar{x}(t)$  (black lines) in the whole gap and  $\bar{x}^i(t)$  (grey lines) in slice  $i$ . (a)  $\tau_m/T = 0.8$ ,  $T = 500$  s; (b)  $\tau_m/T = 60$ ,  $T = 6.66$  s; (a) and (b):  $A = 20$  mm;  $H = 0.4$  mm;  $D_m = 4 \cdot 10^{-4} \text{ mm}^2 \text{ s}^{-1}$ .

from the center of the gap (from slice 0 to slice 4). For all slices and for  $\bar{x}(t)$ , the phase shift of  $\bar{x}$  and  $\bar{x}^i$  with respect to the oscillations of the fluid is zero within experimental error, except for the slice nearest to the walls for which the phase lag is  $\approx 16^\circ$ .

The two regimes and the transition between them are characterized quantitatively by Fig. 12 displaying the variations of the normalized amplitudes  $\bar{x}/A$  and  $\bar{x}^i/A$  as a function of  $\tau_m/T$ . The transition takes place essentially over the same range of values  $2 \leq \tau_m/T \leq 20$  as for  $l_D/A$  in Fig. 5.

In the Taylor regime, for  $\tau_m/T \leq 1$ , all the values of  $\bar{x}/A$  and  $\bar{x}^i/A$  are equal to 1 showing that all parts of the front move at the mean velocity  $\langle v_x(z) \rangle_z$  of the fluid (corresponding to the displacement  $A$ ) and not at the local velocity  $v_x(z)$ .

In the partial reversibility regime, for  $\tau_m/T \geq 20$ ,  $\bar{x}/A$  remains equal to 1 but the local displacements  $\bar{x}^i$  decrease with the distance  $z$  of the slice  $i$  from the center of the gap: this variation corresponds to that of the local amplitude  $A(z)$  of the displacement of the fluid which is proportional to the local fluid velocity and satisfies

$$A(z) = \frac{3A}{2} \left( 1 - 4 \frac{z^2}{H^2} \right). \tag{15}$$

The horizontal dotted lines correspond to the normalized averages  $\langle A(z) \rangle_i/A$  of this amplitude over the range of  $z$  values occupied by each slice: these averages are practically equal to the corresponding values of  $\bar{x}^i$  in the limit of large ratios  $\tau_m/T$  (except for slice 4 for which these values coincide only for  $\tau_m/T \gtrsim 100$ ). For instance, for slice 0,  $\bar{x}^0 = 3A/2$  which corresponds to a displacement at the maximum velocity of the Poiseuille profile. Therefore, in this regime, the *local* motion of the front at a given distance  $z$  follows exactly the *local* displacement of the fluid.

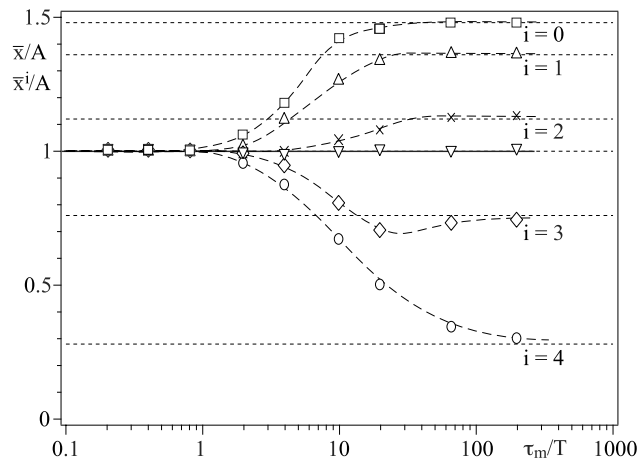


FIG. 12. Variations as a function of  $\tau_m/T$  of the normalized amplitudes  $\bar{x}/A$  and  $\bar{x}^i/A$  of the oscillations  $\bar{x}(t)$  and  $\bar{x}^i(t)$  of the mean displacement of the tracer respectively in the full gap ( $\nabla$ ) and in the slices  $i$  ( $\square$ ,  $\triangle$ ,  $\times$ ,  $\diamond$ ,  $\circ$ ). Dotted horizontal lines: normalized amplitude  $A_i$  of fluid displacement averaged over the corresponding slice. Continuous (dashed) lines: qualitative trends of global (local) the variations.  $A = 20$  mm;  $H = 0.4$  mm;  $D_m = 4 \cdot 10^{-4} \text{ mm}^2 \text{ s}^{-1}$ .

These different results will allow us to explain the oscillations with time (or  $x_r$ ) of the global mean square width  $\overline{\Delta x^2}$  at twice the frequency of the flow observed experimentally (Fig. 4) and numerically (Fig. 7).

We have determined, from the numerical simulations, the normalized amplitude  $\overline{\Delta x^2}_{osc}/A^2$  of these oscillations and their phase shift  $\Delta\varphi$  with respect to  $\sin(2\omega t)$  (the mean fluid displacement is  $A \sin(\omega t)$ ). These values are plotted as a function of  $\tau_m/T$  in Fig. 13 (+) symbols): this variation is in excellent agreement with the predictions obtained in the Appendix with the approach of Ref. 11 (continuous line). The experimental measurements also follow the same variation in the range investigated ( $\Delta$  symbols).

In Fig. 13(b), the transition between the Taylor and partial reversibility regimes is marked by a variation of the phase by  $\pi/2$ . Moreover, while the amplitude of the oscillations is proportional to  $\tau_m/T$  in the first case, it is about constant in the second.

In the Taylor-like regime ( $\tau_m/T \lesssim 2$ ), the variation of  $\overline{\Delta x^2}$  with time results exclusively from the variations of Taylor dispersion with those of the flow velocity: it satisfies Eq. (7) as shown in Sec. III C. The values of  $\overline{\Delta x^{2i}}$  follow exactly the same variation in all individual slices: this is due to the constant amplitude and phase of the oscillations of  $\bar{x}^i$ :  $D_{\parallel}$  is therefore the same for all individual slices, which explains why all the corresponding curves in Fig. 7(a) coincide. Eq. (7) predicts a normalized amplitude of the oscillations proportional to  $\tau_m/T$  and a phase  $\Delta\varphi = 0$ , both in agreement, for  $\tau_m/T \leq 2$ , with the variations displayed in Figs. 13(a) and 13(b).

In the partial reversibility regime ( $\tau_m/T > 20$ ), Eq. (10) shows that  $D_{\parallel}/D_m$  no longer depends on the velocity. The mechanism discussed above for the Taylor-like regime no longer contributes therefore to the oscillations of  $\overline{\Delta x^2}/A^2$ : they are due, in this case, to the periodic distortions of the geometry of the front which, as shown above, follows the local motion of the fluid. The corresponding contribution  $\Delta x_c$  to the front width is purely convective and reversible with respect to a change of the flow direction: this mechanism does not influence, therefore, the global increase of  $\overline{\Delta x^2}$  over time lapses  $\gg T$ . The latter is purely due to the diffusive component estimated in Sec. III B.

Assume that the local mean displacement  $\bar{x}(z, t)$  of the tracer is equal to the displacement  $A(z) \sin(\omega t)$  of the fluid (Eq. (15)); the variation of  $\overline{\Delta x^2}$  with time in the partial reversibility regime will satisfy

$$\overline{\Delta x^2}(t) = [\langle A^2(z) \rangle_z - \langle A(z) \rangle_z^2] \sin^2(\omega t). \quad (16)$$

Then,

$$\frac{\overline{\Delta x^2}(t)}{A^2} = \frac{1}{5} \sin^2(\omega t) = \frac{1}{10} (1 - \cos(2\omega t)). \quad (17)$$

Eq. (17) predicts a phase shift  $\Delta\varphi = \pi/2$  and an amplitude constant with  $\tau_m/T$  with a value in agreement with the high frequency limit of the curves in Fig. 13 (see Eq. (A11)).

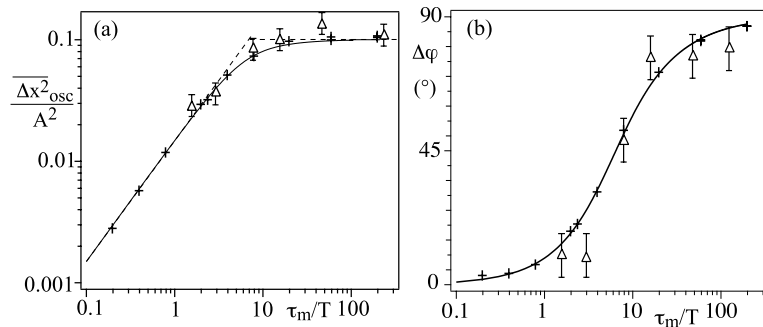


FIG. 13. Variations with  $\tau_m/T$  of the peak to peak normalized amplitude  $\overline{\Delta x^2}_{osc}/A^2$  (a) and phase  $\Delta\varphi$  (b) of the oscillations of period  $T/2$  of  $\overline{\Delta x^2}$ . The phase reference for  $\Delta\varphi$  is the oscillations of the liquid. (+) symbols: values computed from the numerical simulations;  $\Delta$ : experimental values; continuous lines: variations predicted analytically by adapting the results of Ref. 11 (see the Appendix); dotted line: variation of the amplitude from Eqs. (7) and (17).

As shown by Fig. 7, the values  $\overline{\Delta x^2}^i/A^2$  for individual slices do not display oscillations like those of  $\overline{\Delta x^2}/A^2$ , or much weaker ones: this is due to the variations with  $z$  of the local displacement  $x(z)$  which are much smaller across single slices than across the whole gap.

## VI. CONCLUSION

The present experiments and simulations have demonstrated that, except at low Péclet numbers ( $Pe \lesssim 30$ ), the stationary regimes of dispersion in oscillating flows between parallel walls are controlled by the ratio  $\tau_m/T$  (transverse diffusion time/oscillating period): this ratio takes care of the influences of the different characteristic lengths ( $A$  and  $H$ ), of  $T$  and of  $D_m$ . While, for  $\tau_m/T \lesssim 2$ , one has a Taylor-like dispersion with a front width increasing monotonously with time, a new regime appears above  $\tau_m/T \approx 20$ : spreading remains diffusive but is partly reversible during the oscillations. In this latter case, the normalized dispersivity  $l_D/A$  decreases as  $(\tau_m/T)^{-1}$  instead of increasing like  $(\tau_m/T)$ . The time necessary for achieving a Gaussian spreading with a local front width  $\overline{\Delta x^2}$  uniform across the cell gap remains proportional to the diffusion time  $\tau_m$  across it.

The physical origin of these differences is that, when  $\tau_m/T \lesssim 2$ , the characteristic velocity contrast determining the amount of spreading is the mean velocity; if  $\tau_m/T \gtrsim 20$ , it is instead the velocity difference  $\partial v_x/\partial z$  between points separated by the distance  $\Delta z \sim (D_m T)^{1/2}$  across which the tracer diffuses during the period  $T$ . In both regimes, the variation with time of the mean square width  $\overline{\Delta x^2}$  of the diffusion front has an oscillatory component of frequency twice that of the flow oscillations: its origin is however different in the two cases.

For  $\tau_m/T \lesssim 2$ , the oscillations are due to the modulation of the instantaneous dispersion coefficient which is proportional to the square of the velocity: such oscillations are in phase with the absolute value of the fluid displacement and increase linearly with  $\tau_m/T$ . Moreover, all parts of the front oscillate at the same velocity independent of  $z$  and the front remains flat during the oscillations.

For  $\tau_m/T \gtrsim 20$ ,  $D_{\parallel}$  is independent of the velocity and  $\overline{\Delta x^2}$  oscillates because of the periodic stretching of the front by the oscillating Poiseuille velocity profile in the gap: the location  $x(z)$  of the local center of gravity of the tracer follows indeed the oscillations of the local fluid velocity  $v_x(z, t)$ . These two different mechanisms result in a  $\pi/2$  phase shift between the oscillations in the two regimes. Still for  $\tau_m/T \gtrsim 20$ , the oscillatory convective component of the variation of  $\overline{\Delta x^2}$  with the time  $t$  is reversible and does not contribute to the globally linear increase of  $\overline{\Delta x^2}$  with  $t$ .

For still higher values of  $\tau_m/T$ , when the ratio  $\tau_v/T$  becomes large compared to one, one must take into account the influence of the oscillating boundary layers near the walls. This regime was not studied in the present work which deals with dispersion in liquids, for which the Schmidt number  $\nu/D_m$  is large; such effects occur also generally only at high frequencies.

In addition to applications to heat and solute exchange in natural and industrial oscillating flows, such processes suggest an interesting alternative method for measuring molecular diffusion coefficients: using oscillatory flows allows indeed to achieve large travelled lengths (and therefore large front widths  $\Delta x^2$ ) without requiring very long tubes.

An interesting extension of the present study is the influence of a nonzero mean flow: as this flow component increases, one may expect a transition from the dispersion regimes discussed here towards classical Taylor dispersion. In addition to  $\tau_m/T$ , an important characteristic parameter will likely be the ratio of the oscillation amplitude  $A$  and of the path length due to the mean flow during a period  $T$ .

## ACKNOWLEDGMENTS

We acknowledge support by the RTRA Triangle de la Physique, by the LIA PMF-FMF (Franco-Argentinian International Associated Laboratory in the Physics and Mechanics of Fluids) and from UBACyT No. 20020130100570BA. The thesis of Y. L. Roht is supported by a fellowship from the Peruilh foundation of the Faculty of Engineering of the Buenos-Aires University.

## APPENDIX: ANALYTICAL PREDICTION OF THE GLOBAL DISPERSION COEFFICIENT

In order to predict, in the whole range of values of  $\tau_m/T$  of the present work, the macroscopic dispersion for an oscillating flow in a  $HS$  cell, we use the results of Watson<sup>6</sup> on the average diffusion coefficient  $D_{\parallel}$  in the  $HS$  geometry; we also extend to this geometry the work of Chatwin<sup>11</sup> on the time dependence of the diffusion coefficient in a tube or an estuary (shear flow). Chatwin was actually aware of Watson's work on the average macroscopic diffusion coefficient  $D_{\parallel}$  which was published seven years later.

In the  $2D$  geometry of Fig. 6, we assume that the flow is generated by a harmonic pressure gradient  $-G \cos(\omega t)$  in the  $x$  direction giving rise to a velocity  $v_x(z, t) = \Re(f(z)e^{i\omega t})$  along the  $x$  axis in which  $f(z)$  is given by the Navier-Stokes equation,

$$i\omega f = \frac{G}{\rho} + \nu \frac{d^2 f}{dz^2}, \quad (A1)$$

where  $\rho$  is the fluid density,  $\nu$  its kinematic viscosity, and  $f = 0$  on the boundary. The local concentration of contaminant  $c(x, z, t)$  is governed by Eq. (6) with impermeable boundary conditions leading to a solution of the form  $c(x, z, t) = -\gamma x + \Re(\gamma g(z, t)e^{i\omega t})$  such that

$$i\omega g - f = D_m \frac{d^2 g}{dz^2}, \quad (A2)$$

where  $\gamma$  is a constant and  $dg/dz = 0$  on the boundaries. We determine the dispersion coefficient  $D_{\parallel}$ <sup>1</sup> by upscaling Eq. (6) to Eq. (4), *i.e.*, we compute the rate of flux of the contaminant across a  $x$  plane.  $D_{\parallel}$  is then the coefficient of  $-\partial C/\partial x$  where  $C = \bar{c}$  is the average of  $c$  across the gap  $H$ ,

$$D_{\parallel} = D_m + \int \Re(f(z)e^{i\omega t}) \Re((g(z) - \bar{g})e^{i\omega t}) dz/H. \quad (A3)$$

We obtain a time dependent dispersion coefficient with an average value given by Watson<sup>6</sup> and oscillatory components of frequency  $2\omega$  given by Chatwin<sup>11</sup> for a tube and a shear flow. For a Hele-Shaw cell, we obtained using our own notation, the diffusion coefficient and the mean square width,

$$D_{\parallel}(t) = D_m \left[ 1 + R \left( 1 + \frac{A_1}{A_o} \cos(2\omega t) + \frac{A_2}{A_o} \sin(2\omega t) \right) \right], \quad (A4)$$

$$\overline{\Delta x^2} = 2D_m \left[ t + R \left( t + \frac{A_1}{2\omega A_o} \sin(2\omega t) - \frac{A_2}{2\omega A_o} \cos(2\omega t) \right) \right], \quad (A5)$$

where the expression of  $R$  is given in Ref. 6, and we have computed  $A_o$ ,  $A_1$ , and  $A_2$  from Eqs. (A3). These four coefficient function depend on  $\beta = H\sqrt{\omega/2\nu}$ , the ratio of the gap to the thickness of the viscous boundary layer, and  $\beta\sqrt{Sc} = H\sqrt{\omega/2D_m}$ , the ratio of the gap to the thickness of the mass boundary layer. In the above experiments and simulations, the flow oscillations are controlled by the imposed fluid displacement,  $X = A \sin \omega t$  and velocity  $u = A\omega \cos \omega t$  ( $\bar{U} = A\omega$ ) rather than the harmonic pressure gradient. Therefore, the expression of  $R$  involved the  $2D$  tidal volume per unit width along  $y$ ,  $V_t = 2AH$  and

$$R = \frac{A^2}{H^2} \frac{\beta^4 Sc^2 (\cosh \beta - \cos \beta) (C(\beta) - C(\beta\sqrt{Sc}))}{(Sc^2 - 1)(\beta^2(\cos \beta + \cosh \beta) - 2\beta(\sin \beta + \sinh \beta) + 2(\cosh \beta - \cos \beta))} \quad (A6)$$

$$C(\beta) = \frac{\sinh \beta - \sin \beta}{\beta(\cosh \beta - \cos \beta)}.$$

This is the expression used to draw the continuous line in Fig. 5.  $A_o$ ,  $A_1$ , and  $A_2$  are written using the following compact expressions with  $h = (1 + i)\beta/2$ :

$$A_o = \frac{1890}{(Sc^2 - 1)\beta^6} \Re \left[ \frac{i \tanh h}{h} \left( 1 + \frac{\tan h \coth(h\sqrt{Sc})}{\sqrt{Sc}} \right) \right], \quad (A7)$$

$$A_1 + iA_2 = \frac{1890}{iSc\beta^6} \left[ \frac{\tanh^2 h}{h^2} - \frac{Sc(1 - \tanh^2 h)}{2(Sc - 1)} + \frac{(3 - Sc)Sc \tanh h}{2\beta(Sc - 1)^2} - \frac{\sqrt{Sc} \tanh^2 h \coth(h\sqrt{Sc})}{h(Sc - 1)^2} \right].$$

Interesting enough are the limiting cases depending of the frequency. At low frequencies such that,  $\beta = H\sqrt{\omega/2\nu} \ll 1$  and  $\beta\sqrt{Sc} = H\sqrt{\omega/2D_m} \ll 1$ , we do recover the Taylor-like regime,  $A_o = A_1 = 1/2$ ,  $A_2 \ll 1$ ,

$$D_{\parallel} \simeq D_m + D_T \cos^2(\omega t), \text{ in which : } D_T = \frac{(HA\omega)^2}{210 D_m}, \quad (\text{A8})$$

$$\frac{\overline{\Delta x^2}}{A^2} \simeq \frac{\omega \tau_m}{420} [2\omega t + \sin(2\omega t)] + \frac{2t}{\tau_m} \left(\frac{H}{A}\right)^2. \quad (\text{A9})$$

For liquids, the Schmidt number is large (here,  $Sc = 4000$ ) and there exists an intermediate regime where  $\beta \ll 1$ , and  $\beta\sqrt{Sc} \gg 1$ ,  $R \simeq 6A^2/H^2$  and  $A_o \ll A_1, A_2$ . This latter regime is referred to as the ‘‘high frequency’’ or ‘‘partial reversibility’’ regime in the present paper (where the condition  $\beta\sqrt{Sc} \gg 1$  is always assumed to be fulfilled). In this case,

$$D_{\parallel} = D_m \left(1 + 6\frac{A^2}{H^2}\right) + \frac{\omega A^2}{10} \sin(2\omega t), \quad (\text{A10})$$

$$\frac{\overline{\Delta x^2}}{A^2} = \frac{2t}{\tau_m} \left(\frac{H^2}{A^2} + 6\right) - \frac{1}{10} \cos(2\omega t). \quad (\text{A11})$$

The oscillatory term in the last equation is identical to that estimated in Eq. (17). At intermediate values of  $\tau_m/T$ , the phase shift  $\Delta\varphi = \arctan(A_2/A_1)$  varies continuously from 0 to  $\pi/2$  and is plotted on Fig. 13 in good agreement with experiments and simulations.

- <sup>1</sup> G. I. Taylor, ‘‘Dispersion of soluble matter in solvent flowing slowly through a tube,’’ *Proc. R. Soc. A* **219**, 186-203 (1953).
- <sup>2</sup> R. Aris, ‘‘On the dispersion of a solute in a fluid flowing through a tube,’’ *Proc. R. Soc. A* **235**, 67-77 (1956).
- <sup>3</sup> R. Aris, ‘‘On the dispersion of a solute in a pulsating flow through a tube,’’ *Proc. R. Soc. A* **259**, 370-376 (1960).
- <sup>4</sup> I. Ippolito, E. J. Hinch, G. Daccord, and J. P. Hulin, ‘‘Tracer dispersion in 2D fractures with flat and rough walls in a radial flow geometry,’’ *Phys. Fluids A* **5**, 1952-1962 (1993).
- <sup>5</sup> J. Camacho, ‘‘Purely global model for Taylor dispersion,’’ *Phys. Rev. E* **48**, 310-321 (1993).
- <sup>6</sup> E. J. Watson, ‘‘Diffusion in oscillatory pipe flow,’’ *J. Fluid Mech.* **133**, 233-244 (1983).
- <sup>7</sup> C. H. Joshi, R. D. Kamm, J. M. Drazen, and A. S. Slutsky, ‘‘An experimental study of gas exchange in laminar oscillatory flow,’’ *J. Fluid Mech.* **133**, 245-254 (1983).
- <sup>8</sup> M. J. Jaeger and U. H. Kurzweg, ‘‘Determination of the longitudinal dispersion coefficient in flows subjected to high-frequency oscillations,’’ *Phys. Fluids* **26**, 1380-1382 (1983).
- <sup>9</sup> U. H. Kurzweg, G. Howell, and M. J. Jaeger, ‘‘Enhanced dispersion in oscillatory flows,’’ *Phys. Fluids* **27**, 1046-1048 (1984).
- <sup>10</sup> E. R. Holley, D. R. F. Harleman, and H. B. Fischer, ‘‘Dispersion in homogeneous estuary flow,’’ *J. Hydraul. Div. ASCE* **96**, 1691-1709 (1970).
- <sup>11</sup> P. C. Chatwin, ‘‘On the longitudinal dispersion of passive contaminant in oscillatory flows in tubes,’’ *J. Fluid Mech.* **71**, 513-527 (1975).
- <sup>12</sup> H. Yasuda, ‘‘Longitudinal dispersion of matter due to the shear effect of steady and oscillatory currents,’’ *J. Fluid Mech.* **148**, 383-403 (1984).
- <sup>13</sup> R. Smith, ‘‘Contaminant dispersion in oscillatory flows,’’ *J. Fluid Mech.* **114**, 379-398 (1982).
- <sup>14</sup> R. Smith, ‘‘The contraction of contaminant distributions in reversing flows,’’ *J. Fluid Mech.* **129**, 137-151 (1983).
- <sup>15</sup> K. F. Bowden, ‘‘Horizontal mixing in the sea due to a shearing current,’’ *J. Fluid Mech.* **21**, 83-95 (1965).
- <sup>16</sup> R. Smith, ‘‘Dispersion of tracers in the deep ocean,’’ *J. Fluid Mech.* **123**, 131-142 (1982).
- <sup>17</sup> R. W. Horobin and J. A. Kiernan, *Conn’s Biological Stains: A Handbook of Dyes, Stains and Fluorochromes for Use in Biology and Medicine* (Taylor and Francis, Philadelphia, PA, 2002).
- <sup>18</sup> W. B. Russel, D. A. Saville, and W. R. Schowalter, in *Colloidal Dispersions* (Cambridge University Press, Cambridge, UK, 1995), Chap. 3.
- <sup>19</sup> V. J. Charette, E. Evangelista, R. Chertcoff, H. Auradou, J. P. Hulin, and I. Ippolito, ‘‘Influence of the disorder on solute dispersion in a flow channel,’’ *Eur. Phys. J.: Appl. Phys.* **39**, 267-274 (2007).
- <sup>20</sup> A. Boschan, H. Auradou, I. Ippolito, R. Chertcoff, and J. P. Hulin, ‘‘Miscible displacement fronts of shear thinning fluids inside rough fractures,’’ *Water Resour. Res.* **43**, W03438, doi:10.1029/2006WR005324 (2007).
- <sup>21</sup> A. Boschan, I. Ippolito, R. Chertcoff, H. Auradou, L. Talon, and J. P. Hulin, ‘‘Geometrical and Taylor dispersion in a fracture with random obstacles: An experimental study with fluids of different rheologies,’’ *Water Resour. Res.* **44**, W06420, doi:10.1029/2007WR006403 (2008).
- <sup>22</sup> G. Bugliarello and E. D. Jackson III, ‘‘Random walk study of convective diffusion,’’ *Proc. ASCE, Eng. Mech. Div.* **90**(EM4), 49-77 (1964).
- <sup>23</sup> L. D. Landau and E. M. Lifshitz, *Fluid Mechanics*, 2nd ed. (Pergamon Press, Oxford, UK, 1987), Part II, Section 24, Problem 4.
- <sup>24</sup> E. Guyon, J.-P. Hulin, L. Petit, and C. D. Mitescu, in *Physical Hydrodynamics*, 2nd ed. (Oxford Press, Oxford, UK, 2015), Chap. 4.